Investigations with Various Inner Shielding Distance Tests for a Novel Coupler-based CPT System Applied for Electric Vehicles Using Electromagnetic Resonant Coupling and Aluminium Shielding Material

Investigations with Various Inner Shielding Distance Tests for a Novel Coupler-based CPT System Applied for Electric Vehicles Using Electromagnetic Resonant Coupling and Aluminium Shielding Material

J Duan[1,*] and W Wang[2]

[1,2] Department of Engineering and Design, University of Sussex, Brighton BN1 9QT, United Kingdom

*Email: J.Duan@sussex.ac.uk

Abstract. Contactless power transfer (CPT) technology development has been driven rapidly over the past decade by the world-wide trends towards new energy explorations, and numerous reports have been presented in this area. This paper focuses on passive magnetic shielding, which acts as one of the major factors mainly determining the overall CPT system performance when discussing electromagnetic field flux distribution and its real-time effects on magnetic resonant coupling. As a well performance conductive metallic material, aluminium has been adopted to be a passive shielding material in the designed novel H-shape coupler CPT system in this paper, in order to evaluate and find out the optimal inner shielding distance in between the coil and the inner shielding shell. Three inner shielding distances are applied and analyzed across a critical range of system operating frequency, by which the actual CPT system performance differences from perspectives of electromagnetics and power electronics have been illustrated and compared. As a result, it can be noticed that the 15-mm inner shielding gap CPT model is able to yield an optimal system performance with a maximum system efficiency, peak system output RMS power of over 36% and 22 kW, respectively, which also shows an optimal capability to address major concerns over electric vehicle contactless charging. Besides, along with the electromagnetic field parameters generated in the model, such as actual real-time values of flux linkage, magnetic flux density and field strength, it can be found that the 15-mm inner shielding gap prototype is able to achieve better overall magnetic field performance than 5-mm and 25-mm inner shielding distance CPT models.

1. Introduction

Inductive coupling based technologies have been gaining considerable attentions in consumer electronics, factory automations, medical implants, lightings, defense systems and electric vehicles [1]-[4]. Based on inductive coupling principles, contactless power transfer (CPT) has also been proposed more than a decade to mainly address relatively high-power transfer issues and to achieve industrial applications, such as electric vehicles (EV) charging with contactless methods. To cancel out reactive powers from loosely coupler coils to improve system real AC power, compensation topologies have been systematically evaluated in [5]. In this paper, considering inductive coupling via air space or cores could be nonlinear scenarios due to permeability μ and B-H relations of the specific materials used within the coupling module, a proposed H-shape coupler CPT system with aluminium shielding method is introduced to analyze and evaluate the system performance differences in terms of

inner shielding distance changes, based on electromagnetics and 3D finite element methods (FEM). Thus, the induced currents, system output RMS real power, and system power transfer efficiency as power electronics indices, along with the flux linkage, magnetic flux density, magnetic field strength and flux line distribution have been investigated in this paper. The overall system performances of 5-mm, 15-mm and 25-mm inner shielding gap CPT models have been analyzed and compared.

2. CPT system design

Based on the effectiveness of high permeability and low core loss of soft ferromagnetic materials, the geometrically improved H-shape soft magnetic core coupler is proposed to form magnetic flux line trajectories and enhance flux distributions within the inductive coupling space in and between the cores and coils, which can lead to optimal CPT system coupling performance especially at electromagnetic resonant coupling status [6]. Figure 1 presents a stationary contactless power transfer system deploying H-shape ferromagnetic cores with a relative permeability μ of 1000, semi-enclosed combined aluminium shielding and four compensation topologies connecting to both sides of the coupling modular. Due to contributions of minimizing reactance magnitude, the S-S compensation topology has been adopted in the designed CPT system in this paper, as shown in figure 2.

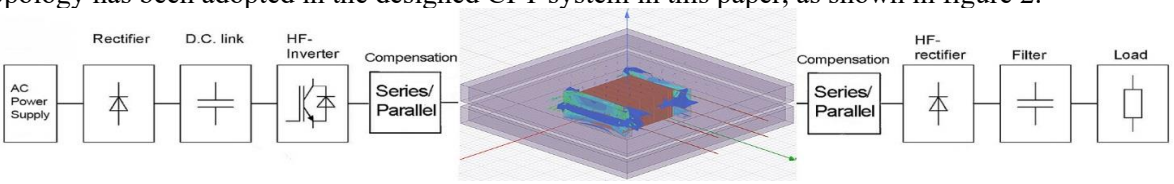

Figure 1. The CPT system configuration with H-shape coupler and combined semi-enclosed shielding.

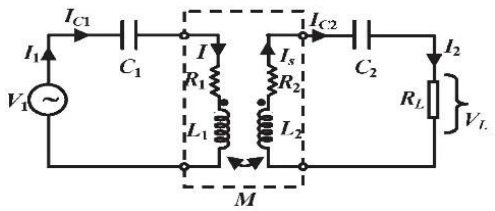

Figure 2. The simplified equivalent circuit of the CPT system with SS compensation topology.

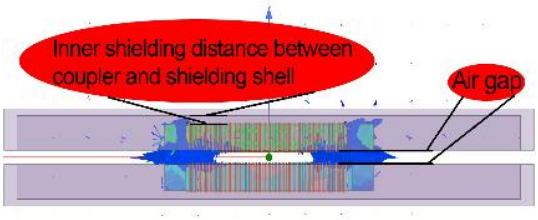

Figure 3. The designed coupler indicating the CPT air gap and the inner shielding distance.

In order to properly produce constantly satisfactory magnetic flux generation with electromagnetic resonant coupling occurring at specific conditions, the innovatively proposed semi-enclosed combined aluminium shielding method has been utilized to further guide and form the actual magnetic flux due to its effects of preventing energy loss in surrounding air [7] and reducing magnetic field flux leakage to the infinite air space [8]. Moreover, different system outcomes of the proposed CPT system with various inner shielding distances, 5 mm, 15 mm and 25 mm, have been delivered and analyzed from both the electromagnetics and power electronics points of view. The designed coupler modular with

inner shielding gap and air gap is presented in figure 3. And the detailed design characteristics of the small-sized H-shape coupler CPT system with aluminium passive shielding are given in table 1.

Table 1. The specifications of the designed CPT system.

Parameters	Values
Winding size	100 mm x 100 mm x 20 mm
Core size	150 mm x 150 mm x 20 mm
H-shaped core bar size of each side	150 mm x 15 mm x 20 mm
Primary winding number of turns	80 turns
Secondary winding number of turns	80 turns
Air gaps of the CPT charging system	10 mm
Winding material	Litz wire
Shielding size	400 mm x 400 x 30 mm
Shielding thickness	10 mm
Inner distance between shielding and coil	5 mm
Passive magnetic shielding materials	Aluminium
Relative permeability μ of core material	1000
Relative permeability μ of shielding material	1.000021
S-S compensation capacitors	150 nF
Load resistor	50 ohm
Voltage power supply	RMS 5 kV
Inner shielding distance between coil and shell	5 mm, 15 mm and 25 mm

3. Electromagnetics principles and numerical representations for the designed CPT system

To analyze the CPT system outputs, in electromagnetic field, the electric current density **J** induced on the secondary side needs be determined. Hence, the Maxwell equations constitutively expressed by Ampere's law in equation (1), Gauss' law in equation (2), Faraday's law in equation (3) and the B-H curve relation in equation (4) are required to be solved:

$$\nabla \times \mathbf{H} = \mathbf{J} \tag{1}$$

$$\nabla \cdot \mathbf{B} = 0 \tag{2}$$

$$\nabla \times \mathbf{E} = -\frac{\partial \mathbf{B}}{\partial t} \tag{3}$$

$$\mathbf{B} = \mu \mathbf{H} \tag{4}$$

where **H** is the magnetic field strength (A/m), **B** is the magnetic flux density (T), **E** is the electric field strength (V/m), and μ is the permeability non-linearly depending on local value of **B** in $\mathbf{B} = f(\mathbf{H})$. The electric current density **J** is in A/m^2.

$$\mathbf{B} = \nabla \times \mathbf{A} \tag{5}$$

Simultaneously with Ohm's law in electromagnetics by equation (6) and material equations of Pouillet's law by equation (7), the 3D finite-element method (FEM) is adopted to numerically solve Maxwell equations above and the relative material equations, using the methods of discretizing the modelled 3D space by tetrahedrons, translating the differential equations into algebraic equations [9]. The methods of semi-iterative conjugate gradient for each magnetic vector potential **A** [10] and the initial B-H curve corresponding μ can be deployed to determine the flux density **B** by equation (5). Repeatedly, the numerical computations can be completed until the convergence of the element permeability.

$$\mathbf{J} = \boldsymbol{\sigma} \mathbf{E} \tag{6}$$

$$\mathbf{R} = \boldsymbol{\rho}\frac{\mathbf{l}}{\mathbf{C}} \tag{7}$$

where $\boldsymbol{\sigma}$ is the material-dependent parameter conductivity. $\boldsymbol{\rho}$ is the resistivity of the windings. **R** is known as electric resistance of the wire material. $\boldsymbol{l}$ is the total length of the wire. **C** is the cross-sectional area of the wire.

Based on the equations above, equation (1) turns into:

$$\nabla \times (\tfrac{1}{\mu}\nabla \times \mathbf{A}) = \mathbf{J} \tag{8}$$

$$\mathbf{E} = -\nabla\phi - \frac{\partial \mathbf{A}}{\partial t} \tag{9}$$

together with Faraday's law and Lorenz gauge vector potential by equation (9) [11], by using 3D FEM computations, the magnetic flux density **B**, the electric field strength **E** and the magnetic field with values of magnetic flux ϕ in weber can be numerically solved and determined.

In order to determine the self-inductance values of **L** in henry produced by the electromagnetic field on the both sides of the CPT system [12], the relations between the coil current values of i and the flux linkage λ satisfy:

$$\lambda_1 = N_1\phi_1 = L_1 i_1 \tag{10}$$

$$\lambda_2 = N_2\phi_2 = L_2 i_2 \tag{11}$$

$$L = \frac{\lambda}{i} \tag{12}$$

To investigate the actual inductive magnetic coupling outcomes and electromagnetic field performance represented and reflected by the numerical vectors and scalars above, the actual RMS power generations given by equation (13) and the efficiencies given by equation (14) and (15) from the front end to the load end of the CPT system are required to be calculated, compared and analyzed. The cos φ is the power factor (PF) caused by phase difference φ between induced voltage and current waveforms.

$$P_{RMS} = V_{RMS}\, I_{RMS} \left| \cos\varphi \right| \tag{13}$$

$$\eta_{Coupler} = \frac{P_{RMS_{Secondary\ coil}}}{P_{RMS_{Primary\ coil}}} \tag{14}$$

$$\eta_{Overal\ system} = \frac{P_{Load}}{P_{RMS_{Power\ supply}}} \tag{15}$$

4. Results and analysis

4.1. Flux linkage and currents with different inner shielding gaps

In this paper, the proposed H-shape coupler CPT systems with aluminium shielding method and three different inner shielding gaps have been investigated across the major significant range of system operating frequency. By emphasizing on the flux linkage in electromagnetics and the induced current in power electronics, it can be seen that the 5-mm, 15-mm and 25-mm inner shielding gap based prototypes produce different characteristic trends against operating frequency.

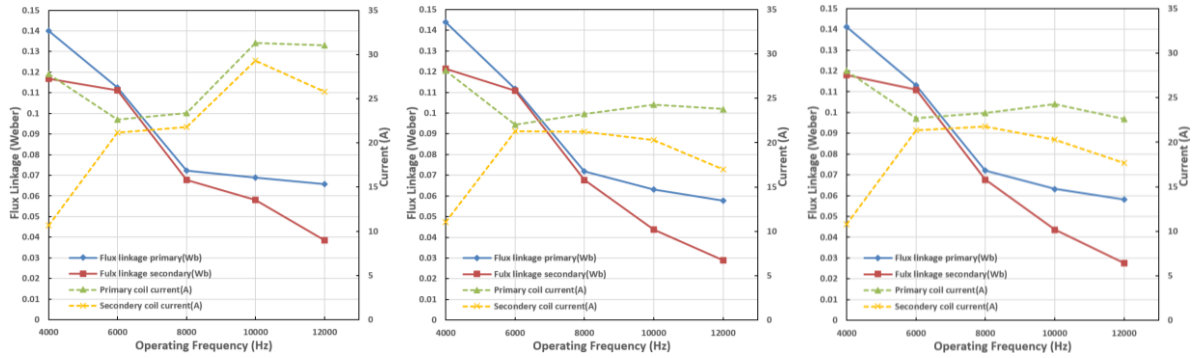

(a) (b) (c)

Figure 4. The flux linkage and current values of the designed CPT system with aluminium shieldingversus system operating frequency. (a) 5-mm inner shielding gap. (b) 15-mm inner shielding gap. (c) 25-mm inner shielding gap.

The results in terms of flux linkage and current have been depicted in figure 4. It can be seen, from figure 4(a), that both the flux linkages of primary and secondary coils tend to drop down against operating frequency despite a more gradual decrease after the frequency point of 8 kHz. In the meantime, the primary coil current shows a slight decrease before 6 kHz and then tends to rise up to a peak value of 31.284 A at 10 kHz. The secondary coil current shows an increasing tendency before 10 kHz as well, reaching its maximum value of 29.292 A. However, the secondary coil current appears to drop down after 10 kHz point, which could be corresponding to the maximum system performance point along with the calculated resonant frequency for the 5-mm inner shielding gap model.

By comparing figure 4(b) and (c), it can be noticed that both the 15-mm and 25-mm inner shielding gap models show very similar tendencies upon flux linkages and coil currents, which may reflect that 15 mm for inner shielding distance could be a critical point due to no further significant differences regarding flux linkage and current against operating frequency with other parameters kept the same in the designed CPT system. Nevertheless, the primary coil currents of both 15-mm and 25-mm inner shielding gap models appear to show maximum values of 24.278 A and 24.296 A at 10 kHz. While, the secondary coil currents of both the 15-mm and 25-mm inner shielding gap models tend to achieve optimal values between 6 kHz to 8 kHz, which can reflect that inductive couplings with satisfactory induced currents to secondary side of the system could be reached during this frequency range in order to produce higher real power on the load end.

4.2. Efficiencies and RMS real powers with different inner shielding gaps

The actual real-time phase angles of induced currents and voltages are changeable in both sides of the system, which determines different real-time power factors (PF) and generates variable RMS real power results [6]. After each CPT system model tends to produce AC stabilized output waveforms, the results of RMS power and efficiency can be computed based on equation (13)-(15) in order to be analyzed.

As indispensable indices to evaluate and reflect the CPT system performance, as shown in figure 5, three different inner shielding gaps based models yield different RMS powers and efficiencies. From figure 5(a), it can be seen that the overall system efficiency shows an increasing tendency to reach a maximum value of 27.480% at 10 kHz. At the same operating frequency, the system output power achieves its peak value of 42.899 kW, which indicates the magnetic resonant coupling status tends to occur at its approximate calculated natural resonant frequency of 10 kHz.

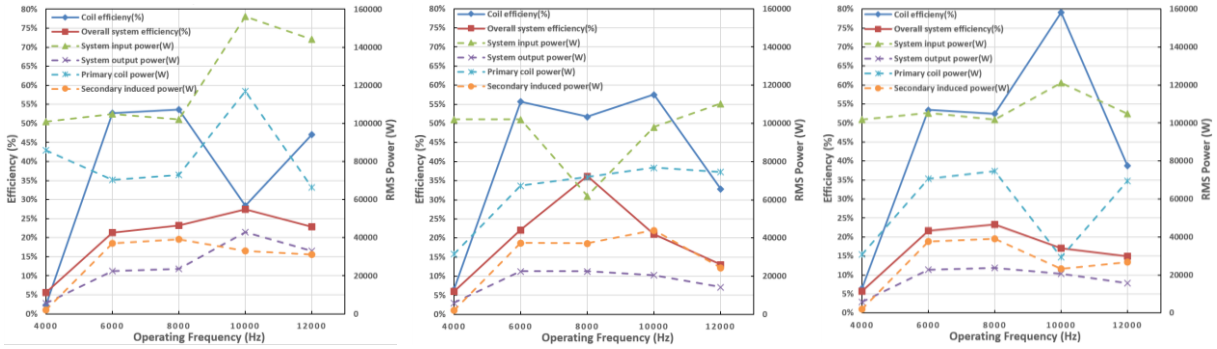

(a) (b) (c)

Figure 5. The RMS real powers and efficiencies of the designed CPT system with aluminium shielding versus system operating frequency. (a) 5-mm inner shielding gap. (b) 15-mm inner shielding gap. (c) 25-mm inner shielding gap.

Regarding the 15-mm inner shielding gap CPT model, it can be noticed, from figure 5(b), that the overall system efficiency shows a sharp peak point at operating frequency of 8 kHz, which indicates a maximum value of 36.257%. Nevertheless, the peak value of the system output power is produced at 6 kHz, which is 22.626 kW. Significantly, it can be found that, across a wide range of operating frequency after 6 kHz, the system output power is able to stay highly satisfactory and sustainable with values of over 20 kW, which reflects that the acceptable electromagnetic field flux distributions and resonant coupling performance in this 5-mm inner shielding gap model enable stable and satisfactory power transfer ratings and overall system efficiencies for the CPT applications to electric vehicles.

In terms of the outcomes of the 25-mm inner shielding gap CPT prototype depicted in figure 5(c), the overall system efficiency tends to be achieved at 8 kHz with a resulted value of 23.245%. In the meantime, the system output power reaches its peak value of 23.676 kW at 8 kHz. By comparison, it can be also found that the average values of overall system efficiency against each operating frequency are almost slightly lower than those of the 5-mm inner shielding gap CPT prototype. Significantly the maximum system efficiency of the third model is much lower than the performance of the 15-mm inner shielding gap CPT prototype, by about 13%, which can reflect and prove that the 15-mm inner shielding gap between coil and inner shell surface can be the optimization for an aluminium passive shielding method.

4.3. Analysis and comparison on main results and field performance with different inner shielding gaps

In addition to graphic tendency comparison and analysis, the detailed major numerical results computed based on theories and equations in previous sections have been illustrated in table 2 for comprehensive evaluations. As can be seen, the overall system efficiency of 15-mm inner shielding gap model shows the best outcomes within these three different inner shielding gap models although the maximum system output power of the 15-mm inner shielding gap model is about 20.27 kW lower than 5-mm inner shielding gap model, which could illustrate and reflect that the latter model can deliver faster charging due to its higher output real power on load. Nevertheless, the 15-mm inner shielding gap model seems more able to produce better efficiency of energy utilization with 36.26% as a peak point. On the other hand, 25-mm inner shielding gap model tends to generate slightly weaker performance than 15-mm one, which could also mean that 15 mm can be the optimal inner shielding gap for the designed CPT system from system efficiency point of view.

Table 2. Main numerical results of the CPT system with three inner shielding distances.

Operating Frequency (Hz)	System with 5-mm inner shielding gap			System with 15-mm inner shielding gap			System with 25-mm inner shielding gap		
	System Output Power (W)	Coil Efficiency	Overall System Efficiency	System Output Power(W)	Coil Efficiency	Overall System Efficiency	System Output Power (W)	Coil Efficiency	Overall System Efficiency
4000	5659.8033	2.2591%	5.6023%	6093.5015	6.6358%	5.9602%	5802.1568	6.4614%	5.7001%
6000	22389.6902	52.7415%	21.3399%	22626.4968	55.6789%	22.1569%	22734.2756	53.4214%	21.6117%
8000	23704.4088	53.6170%	23.2055%	22526.4449	51.8073%	36.2570%	23676.0812	52.3811%	23.2451%
10000	42899.5869	28.3367%	27.4804%	20566.4916	57.5064%	20.9863%	20612.5843	79.1434%	17.0018%
12000	33008.5921	47.0085%	22.9074%	14401.9097	32.9440%	13.0551%	15617.5647	38.6898%	14.9076%

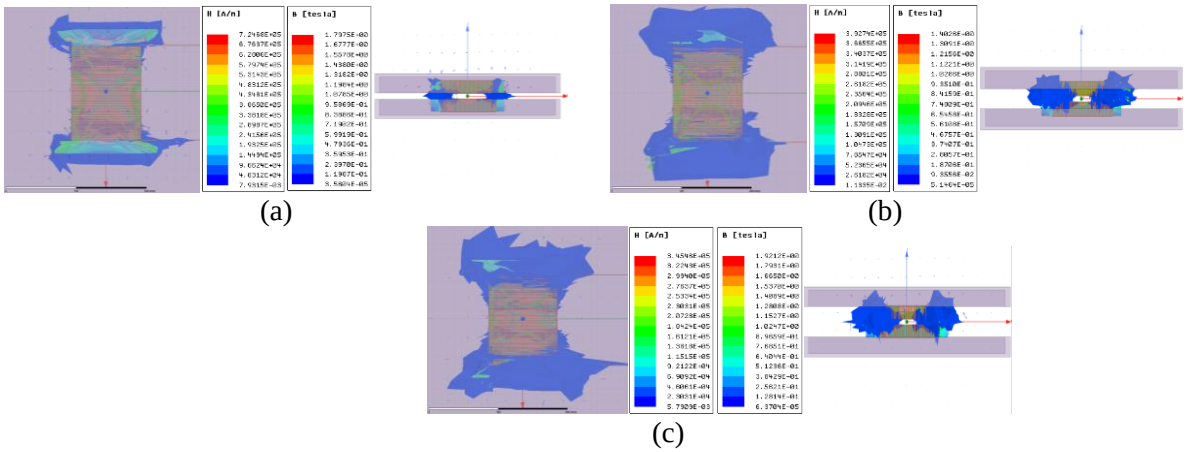

Figure 6. The electromagnetic field distributions of the designed H-shape coupler CPT system with aluminum passive shielding at 1 ms, indicating the magnetic field strength **H** *(A/m)* and the magnetic flux density **B** *(Tesla),* at approximate resonant coupling status as an optimization.(a) The top and left view of the field for 5-mm inner shielding gap. (b) The top and left view for 15-mm inner shielding gap. (c) The top and left view for 15-mm inner shielding gap.

From the perspective of electromagnetics, the magnetic field strength **H** in A/m and the magnetic flux density **B** in Tesla can reflect the field performance of a system based on Maxwell's equations. As can be seen from figure 6, different field flux distributions and parameters are shown to be analyzed. The 5-mm inner shielding gap system can produce maximum **H** and **B** values of 7.2468 x $\mathbf{10^5}$ A/m and 1.7975 Teslas, respectively, at some crucial surface edges and corners of the coupling modular when the system efficiency reaches its maximum of 27.48%. The 15-mm inner shielding gap system can generate maximum **H** and **B** values of 3.9274 x $\mathbf{10^5}$ A/m and 1.4026 Teslas, respectively, when the system tends to be magnetically resonant coupled at 8 kHz as presented in figure 6(b) and table 2. From figure 6(c), it can be seen that the peak values of **H** and **B** field can be 3.4546 x $\mathbf{10^5}$ A/m and 1.4026 Teslas, respectively. Comprehensively, the overall vector values throughout the entire coupling space of the 15-mm inner shielding gap CPT system can be found to be optimized although its **H** and **B** maximum points are slightly weaker than those of the 25-mm inner gap model. Therefore, the 15-mm inner shielding gap can be an optimization from the perspective of electromagnetics.

5. Conclusion

This paper presented a small-sized geometrically improved H-shape coupler CPT system and analyzed performances of using three different inner shielding distances. By focusing on RMS power transfers, CPT system efficiencies, generated electromagnetic field characteristics, it can be found that the 15-mm inner shielding gap can be an optimal shielding method with maximum outputs when considering system power transfer, system efficiency and electromagnetic coupling performance. The 15-mm inner shielding gap CPT system can produce a maximum system efficiency of 36.26%, a peak system output power of 22.63 kW, satisfactory values of magnetic field strength and flux density throughout the coupling modular at about the magnetic resonant frequency.

6. References

[1] Pengfei Li, R. & Bashirullah, 2007. A Wireless Power Interface for Rechargeable Battery Operated Medical Implants. IEEE Transactions on Circuits and Systems II: Express Briefs, 54(10), pp.912–916.
[2] Kawamura, A., 1996. Wireless transmission of power and information through one high-frequency resonant AC link inverter for robot manipulator applications. IEEE Transactions on Industry Applications, 32(3), pp.503–508.
[3] Robertson, D. et al., 2011. High power IPT stage lighting controller. 2011 IEEE International Symposium on Industrial Electronics, pp.1974–1979.
[4] Hui, S.Y.R. & Ho, W.W.C., 2005. A new generation of universal contactless Battery Charging platform for portable Consumer Electronic equipment. IEEE Transactions on Power Electronics, 20(3), pp.620–627.
[5] Sohn, Y. et al., 2015. General Unified Analyses of Two-Capacitor Inductive Power Transfer Systems: Equivalence of Current-Source SS and SP Compensations. IEEE Transactions on Power Electronics, 30(11), pp.6030–6045.
[6] Duan, J., Wang, W., 2018. Electromagnetic Coupling Optimization by Coil Design Improvements for Contactless Power Transfer of Electric Vehicles. In Proceedings of the Future Technologies Conference (FTC) 2018. Advances in Intelligent Systems and Computing, vol 881, (2018) pp. 944-958. Springer, Cham, Switzerland. DOI= https://doi.org/10.1007/978-3-030-02683-7_69
[7] Paul, C.R., Introduction to electromagnetic compatibility, New York: Wiley, 1992.
[8] Wohlfarth, E.P., Ferromagnetic materials: a handbook on the properties of magnetically ordered substances, Amsterdam: North-Holland, 1982.
[9] Sadiku, M., Numerical techniques in electromagnetics, Boca Raton: CRC P, 1992.
[10] Silvester, P., Ferrari, R., Finite elements for electrical engineers (2nd ed.). C.U.P, 1990.
[11] Jackson, J.D. & Okun, L.B., 2000. Historical roots of gauge invariance. Reviews of ModernPhysics, 73(3), pp.663–680.
[12] Grover, F., Inductance Calculations: Working Formulas and Tables. Dover, 1962.